

Direct 3D microprinting of highly conductive gold structures via localized electrodeposition

Patrik Schürch^{a,1}, David Osenberg^{b,1}, Paolo Testa^a, Gerhard Bürki^b, Jakob Schwiedrzik^b, Johann Michler^b, Wabe W. Koelmans^{a,*}

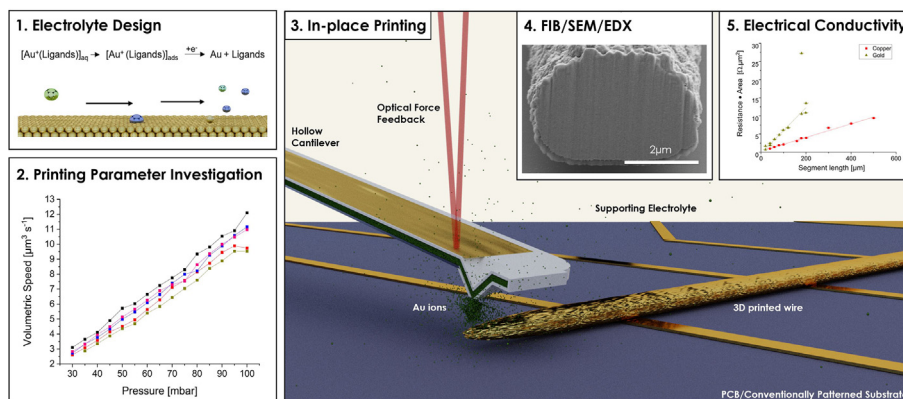
^a Exaddon AG, Sägereistrasse 25, 8152 Glattbrugg, Switzerland

^b Empa, Swiss Federal Laboratories for Materials Science and Technology, Laboratory of Mechanics of Materials and Nanostructures, Feuerwerkerstrasse 39, 3602 Thun, Switzerland

HIGHLIGHTS

- A room-temperature, 3D microprinting process is introduced that produces void-free gold microstructures using localized electrodeposition and cyanide-free chemistry.
- The vertical printing rate of the gold is controlled using the electrodeposition potential and goes up to $1.2 \mu\text{m s}^{-1}$.
- The printing throughput of the gold is controlled using air pressure and reaches up to $20 \mu\text{m}^3 \text{s}^{-1}$.
- The as-deposited resistivity of the gold is 2.5 times higher than bulk and that of the copper only 10 % higher than bulk.

GRAPHICAL ABSTRACT



ARTICLE INFO

Article history:

Received 26 August 2022

Revised 6 February 2023

Accepted 19 February 2023

Available online 21 February 2023

Keywords:

3D microprinting

Additive micromanufacturing

Electrodeposition

Electrochemical 3D printing

Conductivity

FluidFM

ABSTRACT

Directly 3D-printed metal microstructures could enable hybrid micromanufacturing, combining conventional micromanufacturing with additive micromanufacturing (μAM). The microstructure's material properties, including the electrical resistivity, are of decisive importance for a wide range of applications in microelectronics, high-frequency communication, and biomedical engineering. In this work, we present a room-temperature process for μAM of gold structures based on local electrodeposition. We demonstrate control of the electrodeposition process by regulating the precursor species supply rate through air pressure and by regulating the reaction rate through the electrodeposition potential. We 3D printed complex gold microscale structures and characterized the resistivity of the printed gold by developing hybrid devices with integrated four-point probe measurement capability. Additionally, we printed copper microwires, building on a previously shown copper μAM process, and characterized the copper resistivity. We demonstrate near-bulk resistivity values of $65 \text{ n}\Omega\cdot\text{m}$ (about 2.5 times higher than bulk) and $19 \text{ n}\Omega\cdot\text{m}$ (only 10% higher than bulk) for the gold and copper wires, respectively, without post-treatment. Microstructural analysis of the gold wires revealed a dense metal deposit free of voids. Finally, we printed gold structures on a pre-patterned substrate, paving the way to hybrid devices in which additive micromanufacturing is combined with existing micromanufacturing techniques.

© 2023 The Authors. Published by Elsevier Ltd. This is an open access article under the CC BY license (<http://creativecommons.org/licenses/by/4.0/>).

* Corresponding author.

E-mail address: wabe.koelmans@exaddon.com (W.W. Koelmans).

¹ Equal contribution.

1. Introduction

Additive micromanufacturing (μ AM) of metals is a rapidly growing research field with the dedicated goal of complementing existing (photolithographic) microfabrication processes with bespoke, template-free 3D printed structures at the microscale. Typically, μ AM techniques produce a metal quality inferior to that of established 2D microfabrication processes in exchange for added design freedom in the third dimension. For a 3D printing technique to be of practical use for applications, the material quality it produces is essential. However, as μ AM methods for metal are maturing, the demands on new methods proposed become more all-encompassing. These demands include creating complex, freeform 3D structures at the microscale. Here, the degree of overhang, the aspect-ratio that is achievable and the ability to manufacture complex, 3D bodies play a crucial role. Moreover, the throughput of the method should not be prohibitive for larger 3D bodies while yielding a high surface quality and excellent control of the printed structures to deliver the desired material properties. At the microscale, structures can often not be handled and relocated after fabrication, and hence, need to be printed in-place. The requirements posed on the target device and any other required processing step become key elements in the adoption of any μ AM method.

At the same time, pre- and postprocessing to enhance material properties should not be needed or kept to a minimum. For example, high-temperature annealing is a commonly used postprocessing step that is unacceptable for thermally sensitive substrates, such as copper-based microchips or flexible polymeric substrates [1–3].

Amongst the material properties, electrical conductivity is one of the most important characteristics of any metal intended for use in a given application. Extensive effort is made to make μ AM methods reach electrical conductivity values approaching those of conventional microfabrication processes that use e.g., metal evaporation or conventional 2D electrodeposition [4]. The large range of metal μ AM methods that recently was developed, has been comprehensively reviewed and rated for most of the application-relevant requirements, including their electrical conductivity [4,5].

Singling out a top-performing μ AM method in terms of electrical conductivity, we mention meniscus-confined electrodeposition (MCED) that showed an as-deposited copper resistivity down to about 30 n Ω -m (80 % higher than bulk copper) [6,7]. MCED also shows promise in control of the metal microstructure, which underlies the electrical conductivity, by producing parallel arrays of twin grain boundaries [8]. MCED typically produces wire-like objects and is therefore not able to produce complex and overhanging 3D bodies. The wire growth rate goes up to 250 nm s⁻¹ [7].

After silver [9] and copper, gold is the most conductive metal at room temperature. Gold also stands out due to superior plasmonic characteristics resulting from high optical conductivity and chemical inertness [10]. Therefore, gold has applications in many fields, such as photonics [11,12], plasmonics [13,14], microelectronics [15], battery science [16], biomedical engineering [1,2], and electrochemical catalysis [17,18]. Hence, the possibility to additively sculpt gold structures in three dimensions, such as microelectrodes, microneedles [19], nano- and microwires, GHz and THz frequency components [20,21], and photonic elements enables new functionality and superior device performance.

A plethora of methods is available to create gold microstructures [11,13,17,18,22–26]. Restricting the discussion to template-free, μ AM methods, we mention gold structures that were achieved by adding gold chloride into the resin used in two-photon polymerization (2PP) [26]. 2PP is a 3D version of traditional lithography and the authors showed – after thermal annealing at

200 °C – that the resistivity of their gold wires was approximately 50 times higher than bulk gold. The printing of gold was also achieved using gold droplets in a method called laser-induced forward transfer (LIFT), without reporting on the gold resistivity [15]. Resistivity values for LIFT-deposited copper were measured at twelve times the value of bulk resistivity [27]. Much lower resistivity for gold was recently achieved using electrohydrodynamic printing (EHDP). The measurements showed a resistivity down to 50 n Ω -m, or about 2.5 times higher than bulk gold, albeit after sintering at 400 °C, which also led to an object shrinkage to about 27 % of the original volume [9].

Here, we present electrochemical (EC) 3D printing with a system called CERES (Exaddon AG, Switzerland) [28–31]. EC 3D printing is performed inside a supporting electrolyte bath and the EC reaction is confined by locally ejecting a metal electrolyte from a 300-nm-diameter nozzle. The nozzle is an atomic-force-microscope cantilever that we term iontip (Exaddon AG, Switzerland). The iontips have buried microfluidic channels, like the FluidFM cantilevers [32,33]. Recently, FluidFM cantilevers were used to 3D nanoprint reactive polymers [34].

EC 3D printing offers various advantages: 1) The deposition takes place under ambient conditions, with minimal waste. 2) It is a template-free process that is not limited to printing wire-like objects and walls. The design space includes 3D bodies of seamlessly merged voxels, 90-degree overhangs and aspect ratios of over 50, on both flat and non-flat substrates. 3) No postprocessing is necessary to obtain a void-free material with the desired microstructure [5,30]. 4) EC deposition steps are fully compatible with integrated-circuit packaging and printed circuit boards (PCB) production processes. 5) EC 3D printing offers a medium-to-high deposition rate that can be adjusted in conjunction with the print resolution by controlling the printing pressure and the applied potential [20]. Vertical growth rates for copper are in the range of 500 nm s⁻¹ to well beyond 2000 nm s⁻¹ and the throughput exceeds 200 μ m³ s⁻¹ [19].

In this work, we introduce a 3D microprinting method for gold, based on EC 3D printing. We developed a two-component electrolyte system, consisting of a cyanide-free gold electrolyte and an alkaline supporting electrolyte. We demonstrate control of the speed and resolution of the printing process by regulating the overpotential and gold electrolyte flow. We present a method to 3D microprint highly pure, void-free, gold microstructures with electrical conductivity that is at the same level as established 2D electroplating. In parallel, we expand the material study on EC 3D copper characterizing its resistivity using an integrated four-point probe measurement protocol specifically designed for EC 3D printing. The copper resistivity is shown to be a mere 10 % higher than bulk copper resistivity.

Finally, we show the promise and viability of the 3D microprinting approach to design hybrid devices by printing large, complex 3D structures directly onto a PCB.

2. Methods

2.1. Additive micromanufacturing using localized electrodeposition

At the process' core is an AFM cantilever with a built-in microchannel. On the business end of the microchannel is a 300-nm-diameter aperture and on the other end is a reservoir filled with an electrolyte that contains metal ions. The ensemble is referred to as iontip [28]. The iontip is immersed in a supporting electrolyte, which is placed in a three-electrode electrochemical cell (Fig. 1). The substrate and, by extension, the 3D printed structure itself function as the working electrode. An applied air

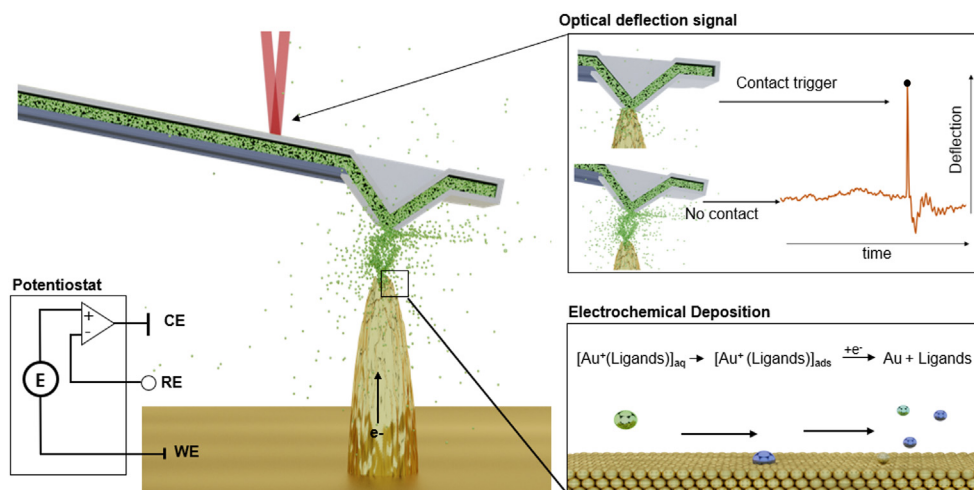


Fig. 1. 3D microprinting schematic showing the substrate that acts as working electrode (WE), the Ag/AgCl reference electrode (RE) and the counter electrode (CE). The iontip is schematically shown in grey and the gold ions in green. Top right inset, the optical beam deflection signal with and without contact. Bottom right inset, simplified schematic of the gold deposition.

pressure advances the electrolyte from the reservoir through the iontip's aperture into the three-electrode cell. Upon reaching the working electrode, the metal ions reduce to solid metal (bottom right inset of Fig. 1).

To ensure the iontip is in the vicinity of the working electrode, the concept of voxels is introduced. The iontip is moved to a specific distance from the working electrode. This distance is termed voxel height, which is typically 0.5 μm to 2 μm . Then, air pressure is applied to the electrolyte-containing reservoir and electrodeposition begins as metal ions reach the working electrode surface. The voxel is considered completed if the metal deposit has grown from the substrate to the iontip aperture. Tip-metal contact is detected by standard optical beam deflection (top right inset of Fig. 1). When the amount of deflection surpasses a trigger threshold (orange dot), then the iontip is moved to the next voxel's location. This printing method provides real-time measurements of each voxel's deposition time.

To print gold, the electrochemical chamber is filled with supporting electrolyte (0.1 M KCl at pH 12) and the iontip is filled with a thiosulfate/sulfite-based gold electrolyte with a gold concentration of 0.5 M, we term the latter gold ink. The gold complexes are reduced into metal at the working electrode. The gold ink is based on the work of Green *et al.* [35], Osaka *et al.* [36,37], and Estrine *et al.* [38]. Gold thiosulfate is used as a base chemical and sodium sulfite is added to create the following two gold thiosulfate/sulfite complexes: $[Au(S_2O_3)(SO_3)_2]^{5-}$ and $[Au(S_2O_3)(SO_3)]^{3-}$ [35]. The pH of the gold ink is adjusted to 12 to avoid a discrepancy in pH between the supporting electrolyte and the ink. Additionally, a pH of 12 decreases the rate of precipitation of colloidal sulfur and gold compared to neutral pH thiosulfate/sulfite-based plating solutions [37]. A prepared batch of ink was stable for up to four weeks.

3. Results and discussion

3.1. Electrochemical 3D microprinting process

The microprinting process is governed by sourcing and consuming precursor species. The source is the flow of ions through the aperture, which is controlled by the air pressure applied to the electrolyte reservoir. The consumption is controlled by the applied

deposition potential. We printed an array of 59 gold micropillars varying both the pressure and the potential (Fig. 2) to investigate the control that can be exercised over the printing process.

For each pillar 80 voxels were used, all with a height of 0.5 μm , and the resulting (maximum) pillar diameter was measured using SEM images (Fig. 2d). The pillar diameter serves as a proxy for voxel diameter, as the determination of the diameter of a single voxel is conceptually not possible because a voxel is merely defined as a height boundary to a local electrodeposition step. The 3D shape of a voxel is therefore not only a function of the potential and pressure varied here, but also a strong function of the local shape of the working electrode surface. The range of the pillar diameter was from 2 μm to 4.5 μm for a pressure range of 30 to 100 mbar (Fig. 2a).

Fig. 2b shows the vertical growth speed of a pillar as a function of pressure and potential. The vertical speed increases with pressure if there is a mass-transport limitation (shortage of precursor species). After a certain pressure, the so-called saturation pressure, has been reached, the vertical speed plateaus. As expected, this vertical speed rises with the deposition potential. Even if the saturation pressure has been reached, the diameter of the pillar still increases with higher pressure (Fig. 2a). Consequently, the volumetric printing speed continues to rise (Fig. 2c). The volumetric speed scales linearly with pressure over the examined range. We conclude from this linearity that the flowrate of precursors species also scales linearly with pressure, and that the efficiency is approximately constant over the range of investigated pressures at a given potential. By efficiency, we mean the amount of reduced precursor below the tip per the total amount of precursor that flowed out of the tip. The applied potential changes this efficiency, as the curves at different potentials appear to be shifted. We attribute the higher efficiency observed at higher overpotential to less precursor diffusion, i.e., more precursors are consumed before they can diffuse away from the working electrode.

The volumetric deposition speed in our experiment reached $11 \mu\text{m}^3\text{s}^{-1}$ and was pushed further to $20 \mu\text{m}^3\text{s}^{-1}$ for the microwire printing. The maximum pillar diameters are achieved at the highest pressure in combination with the lowest vertical speed whereas the thinnest pillars were made at the highest vertical speed and lowest pressure. Qualitatively, the gold deposition described so far follows the description of the copper deposition laid out in previous work [28,29].

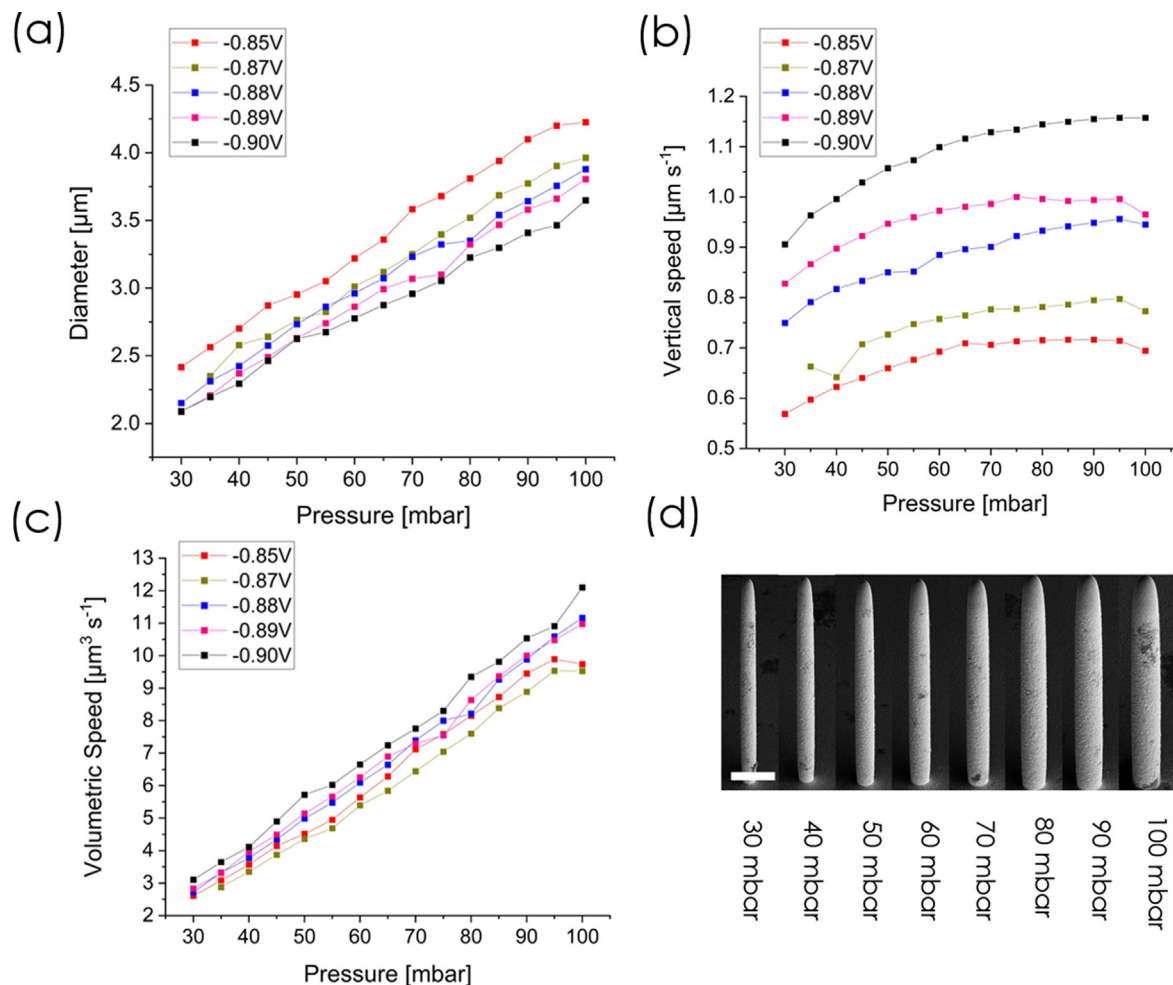


Fig. 2. (a) Measured pillar diameter vs air pressure for different applied potentials (V vs Ag/AgCl). (b) Measured vertical printing speed vs air pressure at different potentials. (c) Calculated volumetric printing speeds vs air pressure at different potentials. (d) Selection of SEM images of pillars printed at -0.87 V vs Ag/AgCl. Scale bar, $4 \mu\text{m}$.

The surface of the pillars is of an excellent quality at lower speeds, even without the use of additives (Fig. 2d). The voxel height of $0.5 \mu\text{m}$ does not leave a visible pattern but yields a dense pillar with a regular diameter along its height. The surface is observed to become rougher with increasing pressure, comparing Fig. 2d–4b, for instance.

3.2. Electrical conductivity

To characterize the electrical properties of the printed material, a test device was conceived. The hybrid test device was made with a conventional photolithographic process (Supporting Fig. 1) and with additive micromanufacturing. Each device has a set of eight, parallel electrodes laid out on a SiO_2 -covered Si substrate. The 100-nm -thick electrodes, made from sputtered gold, are placed at different intervals such that four-point probe measurements can be performed over a range of wire segment lengths. Next, the test device was loaded into the CERES printing system and the deposition potential was applied to the first gold electrode from which the printing of the wire commenced (Fig. 3). From this starting electrode (the bottom electrode in Fig. 3b), a microwire was printed orthogonally across the other seven electrodes and across the SiO_2 layer in between. As the wire print progressed from the first conductive electrode to the non-conductive SiO_2 layer, a large decrease in lateral printing speed was observed (Fig. 3a). The deposition potential and pressure were set such that we obtained a lateral growth speed of approx. $1 \mu\text{m s}^{-1}$ during the seg-

ment atop the SiO_2 . We attribute the observed speed difference to the difference between the local shapes of the working electrode. The efficiency is expected to be much lower for pure lateral growth (atop SiO_2) as compared to combined lateral and vertical growth atop the gold electrode (two insets at the top of Fig. 3a). In other words, in a largely non-conductive environment, many more precursor species diffuse away from the reaction site.

In total, nine test devices were manufactured with three microwires printed out of copper and six microwires printed out of gold. Four-point probe measurements were then performed on multiple wire segments for each microwire. We measured four out of the six gold microwires and all three copper microwires (see Supporting Table 1). The longest gold wires printed (Gold wires 2 and 3) were 2 mm long and, during the electrical measurements, these wires detached from the substrate. We attribute this failure to internal stress in the gold deposit. Therefore, no cross-section data could be gathered, and these wires could not be included in the resistivity study.

In Fig. 4, the measured resistance area product vs the wire segment length is shown. The conductivity values were obtained with a weighted linear fit. The cross sections of the microwires were measured along the entirety of the wire lengths with an optical profilometer (Supporting Figs. 2 and 3). In addition, cross sections were made by focused ion beam (FIB) to correct the optical profilometer data by negating the shadowing effect that causes the optical measurements to overestimate the cross section (Fig. 4b, c and d).

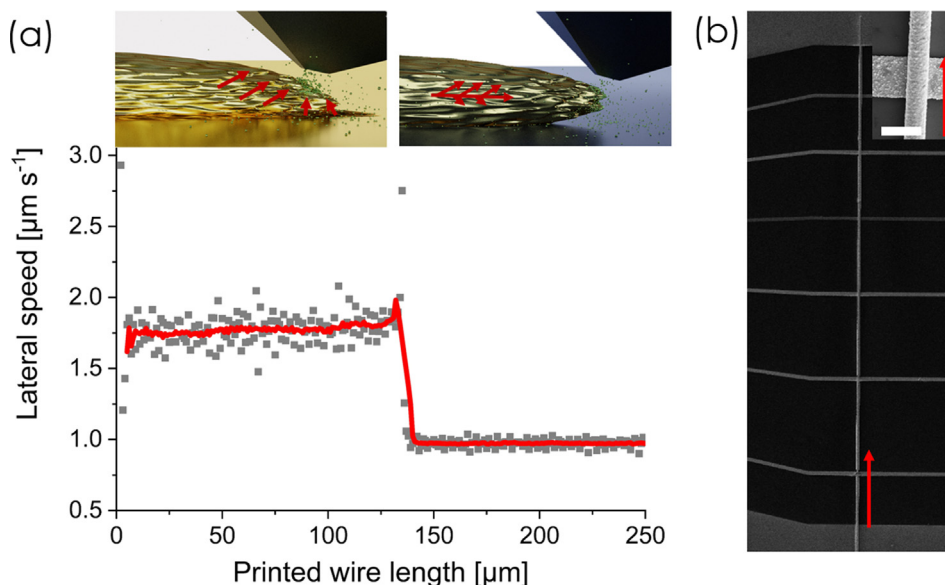


Fig. 3. (a) Lateral printing speed vs printed wire length, showing the drop in printing speed while traversing from the first electrode to the silicon oxide substrate at about 130 μm printed-wire length. A moving average, in red, highlights the drop. The deposition direction is indicated by white arrows. (b) SEM image of a 1500- μm -long gold wire traversing all eight electrodes. Scale bar, 100 μm . The inset shows a zoom of the gold wire crossing an electrode. Scalebar, 10 μm . The printing direction is indicated by red arrows.

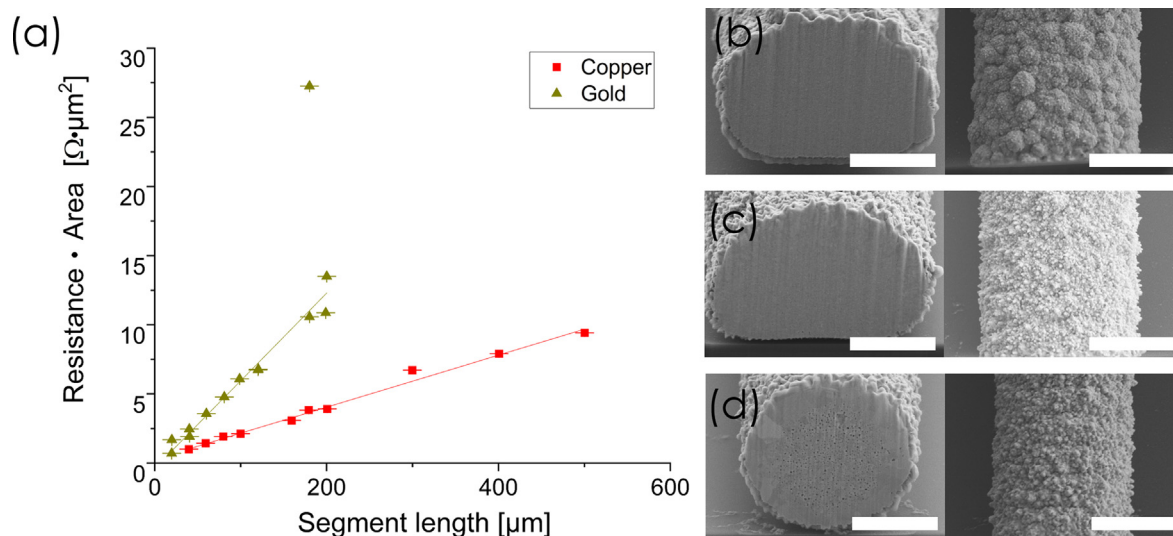


Fig. 4. (a) Resistance times Area of copper and gold microwires vs segment length along wire. (b) Gold Wire 3, cross section (left) and top view (right). (c) Gold Wire 1, cross section (left) and top view (right). (d) Gold Wire 2, cross section (left) and top view (right). (b)–(d) Scale bar, 2 μm .

The copper microwires exhibited excellent resistivity of up to $19 \pm 2 \text{ n}\Omega\cdot\text{m}$. This value is very close to the $18 \text{ n}\Omega\cdot\text{m}$ resistivity reported for copper that is made by laser sintering [39]. Conventionally electrodeposited copper can reach a resistivity of $17 \text{ n}\Omega\cdot\text{m}$ [40].

The resistivity of the electrodeposited gold material was found to be $65 \pm 6 \text{ n}\Omega\cdot\text{m}$. This resistivity is excellent, in the context of gold electrodeposition, considering gold thin films plated from a similar thiosulfate-sulfite solution showed a resistivity of $70 \text{ n}\Omega\cdot\text{m}$ [38]. The outlying data point is most likely due to an undetected bottleneck in the microwire, such as a large pore. For all measurements in Fig. 4a, a low-resistance electrical contact between pad and wire was established and were therefore included in the calculation of the resistivity.

The difference in surface quality between the wire and the pillar is striking; the surface of the pillars is much smoother than the surface of the wires. We ascribe these differences to three causes. Firstly, the pillars were printed on a conductive gold surface. This large gold surface acts as an ion sink for precursor species that diffused away from the iontip will deposit onto. As for the wire, the only surface available for the precursor species to deposit is the already printed gold wire, which increases the amount of additionally plated gold at low ionic concentration. It has been reported for comparable systems [41] that low-concentration deposition can lead to changes in nucleation behavior and, as a result, to changes in surface morphology. Secondly, the convective flow creates different concentration profiles of the metal ions around the iontip because the wire axis is orthogonal to the pillar axis. Based on

Table 1

Gold microwire printing parameters.

Sample name	Deposition voltage [V vs Ag/AgCl]	Average lateral speed [$\mu\text{m s}^{-1}$]	Printing pressure [mbar]	Voxel height [μm]	Total length of the wire [μm]
Gold wire 1	−0.98	1.2	150	2	750
Gold wire 2	−0.98	1.2	150	2	2000
Gold wire 3	−0.90	0.78	150	2	2000
Gold wire 4	−0.96	1.08	180	2	1200
Gold wire 5	−0.96	1.08	180	2	1200
Gold wire 6	−0.94	0.7	85	2	750

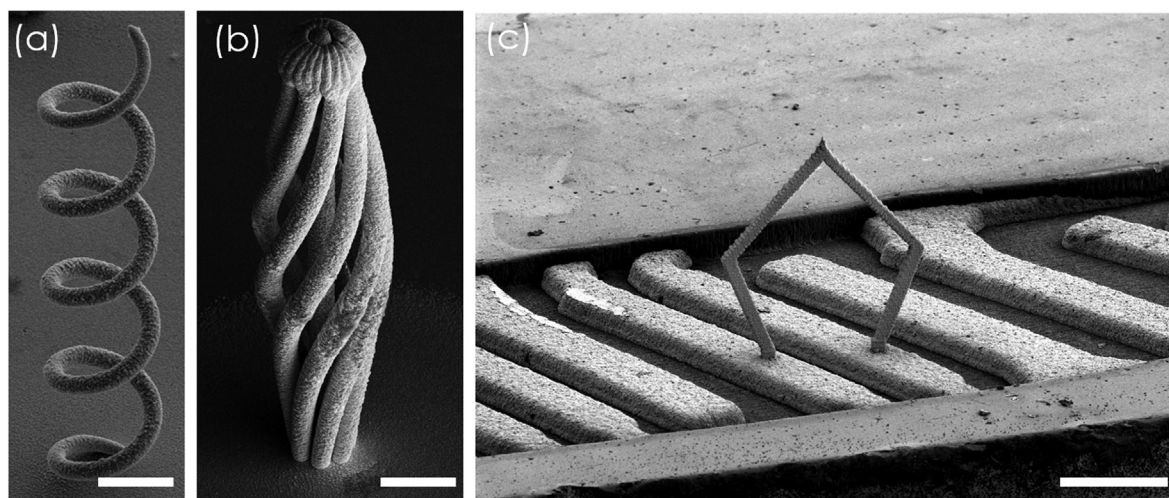


Fig. 5. (a) A gold helix printed on a gold substrate. Scale bar, 10 μm . (b) A microplug printed in gold. Design courtesy of Axon Cables, SA. Scale bar, 20 μm . (c) A gold, pentagon-shaped connector printed on a PCB between two gold pads. Scale bar, 100 μm .

the direction of the convective flow and the lower growth speeds observed for the wires, we expect that the outer shell of the micro-wires is plated at a low ionic concentration by ions that diffused away from the iontip. Thirdly, the applied potential required to obtain a lateral speed of $1 \mu\text{m s}^{-1}$ was significantly higher than the potential required for a vertical speed of $1 \mu\text{m s}^{-1}$ (see Fig. 2a and Table 1). A higher potential also leads to an increased surface roughness and a different surface morphology on the wires.

3.3. Microstructural analysis

Cross sections of the printed gold structures were obtained by FIB to investigate the quality of the printed material. The gold cross sections show no visible porosity at low overpotential but show a substantial amount of porosity at deposition potential $> -1.02 \text{ V. vs Ag/AgCl}$ (Fig. 4d). Most likely the small pores are caused by hydrogen evolution at the growth front, which is the typical reason for porosity in aqueous electrodeposits [42]. The larger pores could have been caused by coarse grains encapsulating electrolyte. Porosity is expected to increase the error in the electrical measurements. When comparing the gold wires to the copper wires, the copper wire cross sections show dense copper with no visible porosity.

Energy-Dispersive X-ray (EDX) analysis (Supporting Figs. 4 and 5) of the wires show gold with carbon, nitrogen, and oxygen and as well as silica. The light elements, carbon, and nitrogen can be almost certainly attributed to surface contamination of the deposited material, as they are not part of the chemical make-up of the electrolyte. The presence of silicon is primarily attributed to the substrate. A secondary source of silicon is the microfluidic channel

inside the cantilever. Likely, other impurities below the EDX detection limit, such as sodium, sulfur, and chloride are present in the ppm range, because they are present in the electrolyte as well. These impurities, even though in low concentrations, might form a significant contribution to the reduced electrical conductivity compared to pure bulk gold.

3.4. Example structures

Multiple structures have been printed as examples. A helical gold structure was printed (see Fig. 5a), like the photonic structures created by Gansel *et al.* [11]. The helical structure has a diameter of $10 \mu\text{m}$ and a $10 \mu\text{m}$ vertical displacement per turn of the helix. The helix has 5 turns and was built with 210 voxels. It was printed at a pressure of 65 mbar and a vertical speed of $1.2 \mu\text{m s}^{-1}$. The printed voxels merge and can visually not be differentiated from each other.

A microplug has been produced at printing speeds of $0.7 \mu\text{m s}^{-1}$ and shows the possibility of 3D capabilities of intertwined single voxel strands which merge to a spherical top (Fig. 5b). The strands were printed at a pressure of 70 mbar and the spherical top at 40 mbar. The structure was built with 1903 voxels.

Finally, a large, pentagon-shaped, connection (Fig. 5c) was printed directly on a printed circuit board (PCB). The connection consists of 18'760 voxels with an average spacing of $2 \mu\text{m}$ between the layers in the Z direction and an inter-strand distance of $1 \mu\text{m}$ in the XY plane. The alignment of the connection with the PCB was done using an optical camera of the CERES system. The tilt of the PCB substrate was measured and corrected for. The structure was printed at a speed of $1 \mu\text{m s}^{-1}$.

4. Conclusion

We have presented a new μ AM process for high-quality gold using a cyanide-free recipe that expands the capabilities of electrochemical 3D microprinting techniques. We designed, fabricated, and characterized microscale 3D structures using the new process. Material analysis shows dense gold with a high purity. Voids appeared only at high electrodeposition potential but are otherwise absent. We have demonstrated that EC 3D printing can bring the electrical conductivity of gold and copper to levels like those produced by established 2D deposition methods. The gold showed a resistivity of $65 \pm 6 \text{ n}\Omega\cdot\text{m}$, which is an excellent value compared to gold that is conventionally electrodeposited out of thiosulfate-based solutions without any post-processing. The copper wires made by EC 3D printing in this work showed a resistivity of merely 10 % above pure bulk copper.

The prospects are intriguing: hybrid devices can be built where microscale copper and gold structures are directly 3D printed, in place, on previously structured devices. Components like micro-wires, coils, plugs, neural interfaces, needles, connectors, and others can be printed precisely onto existing structures with a medium-to-high deposition speed. The integrated electrical connections required to drive such components during their operation are shown to also apply the working electrode potential needed during their 3D microfabrication. Therefore, the need of the EC 3D printing process to have a conductive starting point does not pose design restrictions of significance on either PCBs or silicon dies.

Both gold and copper show promise due to their excellent conductivity. Additionally, micrometer-sized components of gold have enormous potential in biomedical applications, in situ nerve stimulation and action potential recording. Gold is also of significant use for GHz frequency electronics and communications.

The ability of this cyanide-free process to additively manufacture complex 3D structures out of a high-quality gold metal, along with the absence of pre- and postprocessing steps make this μ AM process a promising choice for microsensors, microneedles, actuators, and gold-based electronics.

CRediT authorship contribution statement

Patrik Schürch: Investigation, Validation, Formal analysis, Writing – original draft, Visualization. **David Osenberg:** Methodology, Investigation, Formal analysis, Writing – review & editing. **Paolo Testa:** Investigation, Validation, Writing – review & editing. **Gerhard Bürki:** Investigation. **Jakob Schwiedrzik:** Writing – review & editing, Supervision. **Johann Michler:** Writing – review & editing, Supervision. **Wabe W. Koelmans:** Conceptualization, Writing – original draft, Supervision.

Data availability

Data will be made available on request.

Declaration of Competing Interest

The authors declare that they have no known competing financial interests or personal relationships that could have appeared to influence the work reported in this paper.

Acknowledgements

We thank Giorgio Ercolano for his contribution to the gold electrodeposition recipe and the discussions. Furthermore, we thank

Axon Cables SA for the design of the microplug. The authors thank Edward White for proofreading the manuscript.

Appendix A. Supplementary material

Supplementary data to this article can be found online at <https://doi.org/10.1016/j.matdes.2023.111780>.

References

- [1] J. Agorelius, F. Tsanakalis, A. Friberg, P.T. Thorbergsson, L. Pettersson, J. Schouenborg, An array of highly flexible electrodes with a tailored configuration locked by gelatin during implantation—Initial evaluation in cortex cerebri of awake rats, *Front. Neurosci.* 9 (2015) 331, <https://doi.org/10.3389/fnins.2015.00331>.
- [2] M.D. Tang-Schomer, X. Hu, M. Hronik-Tupaj, L.W. Tien, M.J. Whalen, F.G. Omenetto, D.L. Kaplan, Film-based implants for supporting neuron–electrode integrated interfaces for the brain, *Adv. Funct. Mater.* 24 (2014) 1938–1948, <https://doi.org/10.1002/adfm.201303196>.
- [3] A. Vyatsikh, S. Delalande, A. Kudo, X. Zhang, C.M. Portela, J.R. Greer, Additive manufacturing of 3D nano-architected metals, *Nat. Comm.* 9 (2018) 593, <https://doi.org/10.1038/s41467-018-03071-9>.
- [4] L. Hirt, A. Reiser, R. Spolenak, T. Zambelli, Additive manufacturing of metal structures at the micrometer scale, *Adv. Mat.* 29 (2017) 1604211, <https://doi.org/10.1002/adma.201604211>.
- [5] A. Reiser, L. Koch, K.A. Dunn, T. Matsuura, F. Iwata, O. Fogel, Z. Kotler, N. Zhou, K. Charipar, A. Piqué, P. Rohner, D. Poulikakos, S. Lee, K. Seol, I. Utke, C. Van Nesselroy, T. Zambelli, J.M. Wheeler, R. Spolenak, Metals by micro-scale additive manufacturing: Comparison of microstructure and mechanical properties, *Adv. Funct. Mat.* 30 (2020) 1910491, <https://doi.org/10.1002/adfm.201910491>.
- [6] A.P. Suryavanshi, M.-F. Yu, Probe-based electrochemical fabrication of freestanding Cu nanowire array, *Appl. Phys. Lett.* 88 (2006), <https://doi.org/10.1063/1.2177538> 083103.
- [7] J. Hu, M.-F. Yu, Meniscus-confined three-dimensional electrodeposition for direct writing of wire bonds, *Science* 329 (2010) 313–316, <https://doi.org/10.1126/science.1190496>.
- [8] S. Daryadel, A. Behroozfar, M. Minary-Jolandan, Toward control of microstructure in microscale additive manufacturing of copper using localized electrodeposition, *Adv. Eng. Mat.* 21 (2019) 1800946, <https://doi.org/10.1002/adem.201800946>.
- [9] C. van Nesselroy, C. Shen, T. Zambelli, D. Momotenko, Electrochemical 3D printing of silver and nickel microstructures with FluidFM, *Add. Manufact.* 53 (2022), <https://doi.org/10.1016/j.addma.2022.102718> 102718.
- [10] K. Kolwas, D. Derkachova, Impact of the interband transitions in gold and silver on the dynamics of propagating and localized surface plasmons, *Nanomater.* 10 (2020) 1411, <https://doi.org/10.3390/nano10071411>.
- [11] J.K. Gansel, M. Thiel, M.S. Rill, M. Decker, K. Bade, V. Saile, G. von Freymann, S. Linden, M. Wegener, Gold helix photonic metamaterial as broadband circular polarizer, *Science* 325 (2009) 1513–1515, <https://doi.org/10.1126/science.1177031>.
- [12] J.K. Gansel, M. Latzel, A. Frolich, J. Kaschke, M. Thiel, M. Wegener, Tapered gold-helix metamaterials as improved circular polarizers, *Appl. Phys. Lett.* 100 (2012) 3, <https://doi.org/10.1063/1.3693181>.
- [13] D. Kuhnness, A. Gruber, R. Winkler, J. Sattelkow, H. Fitzek, I. Letofsky-Papst, G. Kothleitner, H. Plank, High-fidelity 3D nanoprinting of plasmonic gold nanoantennas, *ACS Appl. Mater. Interfaces* 13 (2021) 1178–1191, <https://doi.org/10.1021/acsami.0c17030>.
- [14] G. Ruffato, F. Romanato, D. Garoli, S. Cattarin, Nanoporous gold plasmonic structures for sensing applications, *Opt. Express* 19 (2011) 13164–13170, <https://doi.org/10.1364/OE.19.013164>.
- [15] P.T. Bishop, L.J. Ashfield, A. Berzins, A. Boardman, V. Buche, J. Cookson, R.J. Gordon, C. Salcianu, P.A. Sutton, Printed gold for electronic applications, *Gold Bulletin* 43 (2010) 181–188, <https://doi.org/10.1007/BF03214985>.
- [16] C. Xu, B.M. Gallant, P.U. Wunderlich, T. Lohmann, J.R. Greer, Three-dimensional Au microlattices as positive electrodes for Li-O₂ batteries, *ACS Nano* 9 (2015) 5876–5883, <https://doi.org/10.1021/acs.nano.5b00443>.
- [17] P. Rohner, A. Reiser, F.T. Rabouw, A.S. Sologubenko, D.J. Norris, R. Spolenak, D. Poulikakos, 3D electrohydrodynamic printing and characterisation of highly conductive gold nanowalls, *Nanoscale* 12 (2020) 20158–20164, <https://doi.org/10.1039/D0NR04593D>.
- [18] M. Khan, P. Dickens, Selective laser melting (SLM) of pure gold, *Gold Bull.* 43 (2010) 114–121, <https://doi.org/10.1007/BF03214976>.
- [19] R. Sachan, P. Schürch, P. Testa, E. Hepp, W.W. Koelmans, R.J. Narayan, Hollow copper microneedle made by local electrodeposition-based additive manufacturing, *MRS Advances* 6 (2021) 893–896, <https://doi.org/10.1557/s43580-021-00184-0>.
- [20] G. Ulisse, P. Schürch, W.W. Koelmans, V. Krozer, 3D printing of a metallic helix for traveling wave tube amplifiers operating in millimeter wave range, *IRMMW-THz* (2021) 1–2, <https://doi.org/10.1109/IRMMW-THz50926.2021.9567223>.

- [21] S.S. Dhillon et al., The 2017 terahertz science and technology roadmap, *J. Phys. D: Appl. Phys.* 50 (2017), <https://doi.org/10.1088/1361-6463/50/4/043001> 043001.
- [22] M.M. Shawrav, P. Taus, H. Wanzenboeck, M. Schinnerl, M. Stöger-Pollach, S. Schwarz, A. Steiger-Thirsfeld, E. Bertagnolli, Highly conductive and pure gold nanostructures grown by electron beam induced deposition, *Sci. Rep.* 6 (2016) 34003, <https://doi.org/10.1038/srep34003>.
- [23] M. Feinaeugle, R. Pohl, T. Bor, T. Vaneker, G.-W. Römer, Printing of complex free-standing microstructures via laser-induced forward transfer (LIFT) of pure metal thin films, *Add. Manufact.* 24 (2018) 391–399, <https://doi.org/10.1016/j.addma.2018.09.028>.
- [24] A. Weitzer, M. Huth, G. Kothleitner, H. Plank, Expanding FEBID-based 3D-nanoprinting toward closed high-fidelity nanoarchitectures, *ACS Appl. Elec. Mater.* 4 (2022) 744–754, <https://doi.org/10.1021/acsaelm.1c01133>.
- [25] M. Łysień, Ł. Witczak, A. Wiatrowska, K. Fiarczyk, J. Gadzańska, L. Schneider, W. Stręk, M. Karpiński, Ł. Kosior, F. Granek, P. Kowalczewski, High-resolution deposition of conductive and insulating materials at micrometer scale on complex substrates, *Sci. Rep.* 12 (2022) 9327, <https://doi.org/10.1038/s41598-022-13352-5>.
- [26] E. Blasco, J. Müller, P. Müller, V. Trouillet, M. Schön, T. Scherer, C. Barner-Kowollik, M. Wegener, Fabrication of conductive 3D gold-containing microstructures via direct laser writing, *Adv. Mater.* 28 (2015) 3592–3595, <https://doi.org/10.1002/adma.201506126>.
- [27] C.W. Visser, R. Pohl, C. Sun, G.-W. Römer, B. Huis in 't Veld, D. Lohse, Toward 3D printing of pure metals by laser-induced forward transfer, *Adv. Mater.* 27 (2015) 4087–4092, <https://doi.org/10.1002/adma.201501058>.
- [28] G. Ercolano, C. van Nisselroy, T. Merle, J. Vörös, D. Momotenko, W.W. Koelmans, T. Zambelli, Additive manufacturing of sub-micron to sub-mm metal structures with hollow AFM cantilevers, *Micromachines* 11 (2020) 1, <https://doi.org/10.3390/mi11010006>.
- [29] G. Ercolano, T. Zambelli, C. van Nisselroy, D. Momotenko, J. Vörös, T. Merle, W. W. Koelmans, Multiscale additive manufacturing of metal microstructures, *Adv. Eng. Mater.* 22 (2020) 1900961, <https://doi.org/10.1002/adem.201900961>.
- [30] R. Ramachandramoorthy, S. Kalácska, G. Poras, J. Schwiedrzik, T.E.J. Edwards, X. Maeder, T. Merle, G. Ercolano, W.W. Koelmans, J. Michler, Anomalous high strain rate compressive behavior of additively manufactured copper micropillars, *Appl. Mater. Today* 27 (2022), <https://doi.org/10.1016/j.apmt.2022.101415> 101415.
- [31] L. Hirt, S. Ihle, Z. Pan, L. Dorwling-Carter, A. Reiser, J.M. Wheeler, R. Spolenak, J. Vörös, T. Zambelli, Template-free 3D microprinting of metals using a force-controlled nanopipette for layer-by-layer Electrodeposition, *Adv. Mater.* 28 (2016) 2311–2315, <https://doi.org/10.1002/adma.201504967>.
- [32] O. Guillaume-Gentil, E. Potthoff, D. Ossola, C.M. Franz, T. Zambelli, J.A. Vorholt, Force-controlled manipulation of single cells: From AFM to FluidFM, *Trends Biotechnol.* 32 (2014) 381–388, <https://doi.org/10.1016/j.tibtech.2014.04.008>.
- [33] A. Meister, M. Gabi, P. Behr, P. Studer, J. Vörös, P. Niedermann, J. Bitterli, J. Polesel-Maris, M. Liley, H. Heinzelmann, T. Zambelli, FluidFM: Combining atomic force microscopy and nanofluidics in a universal liquid delivery system for single cell applications and beyond, *Nano Lett.* 9 (2009) 2501–2507, <https://doi.org/10.1021/nl901384x>.
- [34] T.G. Pattison, S. Wang, R.D. Miller, G.-Y. Liu, G.G. Qiao, 3D nanoprinting via spatially controlled assembly and polymerization, *Nat. Comm.* 13 (2022) 1941, <https://doi.org/10.1038/s41467-022-29432-z>.
- [35] T.A. Green, M.J. Liew, S. Roy, Electrodeposition of gold from a thiosulfate-sulfite bath for microelectronic applications, *J. Electrochem. Soc.* 150 (2003) C104, <https://doi.org/10.1149/1.1541006>.
- [36] T. Osaka, A. Kodera, T. Misato, T. Homma, Y. Okinaka, O. Yoshioka, Electrodeposition of soft gold from a thiosulfate-sulfite bath for electronics applications, *J. Electrochem. Soc.* 144 (1997) 3462–3469, <https://doi.org/10.1149/1.1838033>.
- [37] T. Osaka, M. Kato, J. Sato, K. Yoshizawa, T. Homma, Y. Okinaka, O. Yoshioka, Mechanism of sulfur inclusion in soft gold electrodeposited from the thiosulfate-sulfite bath, *J. Electrochem. Society* 148 (2001) C659, <https://doi.org/10.1149/1.1399276>.
- [38] E.C. Estrine, S. Riemer, V. Venkatasamy, B.J.H. Stadler, I. Tabakovic, Mechanism and stability study of gold electrodeposition from thiosulfate-sulfite solution, *J. Electrochem. Soc.* 161 (2014) D687–D696, <https://doi.org/10.1149/2.0411412jes>.
- [39] Q. Jiang, P. Zhang, Z. Yu, H. Shi, D. Wu, H. Yan, X. Ye, Q. Lu, Y. Tian, A review on additive manufacturing of pure copper, *Coatings* 11 (2021) 740, <https://doi.org/10.3390/coatings11060740>.
- [40] V.S. Donepudi, R. Venkatachalapathy, P.O. Ozemoyah, C.S. Johnson, J. Prakash, Electrodeposition of copper from sulfate electrolytes: Effects of thiourea on resistivity and electrodeposition mechanism of copper, *Electrochem. Solid-State Lett.* 4 (2001) C13, <https://doi.org/10.1149/1.1342144>.
- [41] D. Grujicic, B. Pesic, Electrodeposition of copper: The nucleation mechanisms, *Electrochim. Acta* 47 (2002) 2901–2912, [https://doi.org/10.1016/S0013-4686\(02\)00161-5](https://doi.org/10.1016/S0013-4686(02)00161-5).
- [42] G. Sanzò, I. Taurino, R. Antiochia, L. Gorton, G. Favero, F. Mazzei, G. De Micheli, S. Carrara, Bubble electrodeposition of gold porous nanocorals for the enzymatic and non-enzymatic detection of glucose, *Bioelectrochemistry* 112 (2016) 125–131, <https://doi.org/10.1016/j.bioelechem.2016.02.012>.